

Numerical Study on the Effects of Montney Formation Stiffness on Injection-Induced Seismicity in Northeastern British Columbia (NTS 093, 094A, B, G, H)

A. Mehrabifard¹, Department of Earth, Ocean and Atmospheric Sciences, The University of British Columbia, Vancouver, British Columbia, amehrabifard@eoas.ubc.ca

E. Eberhardt, Department of Earth, Ocean and Atmospheric Sciences, The University of British Columbia, Vancouver, British Columbia

Mehrabifard, A. and Eberhardt, E. (2022): Numerical study on the effects of Montney Formation stiffness on injection-induced seismicity in northeastern British Columbia (NTS 093, 094A, B, G, H); *in* Geoscience BC Summary of Activities 2021: Energy and Water, Geoscience BC, Report 2022-02, p. 23–34.

Introduction

The Lower Triassic Montney Formation is a really extensive, covering approximately 130 000 km² from central Alberta to northeastern British Columbia (BC; National Energy Board et al., 2013). This gas-bearing shale is also thick, typically ranging from 100 to 300 m, and, although thinning to zero at its eastern and northeastern subcropping margins, increases to over 300 m on its western margin before it begins outcropping in the Rocky Mountains. However, the permeability of this formation is commonly in the 10⁻²¹ to 10⁻¹⁸ m² range. The Montney Formation is considered a prime candidate for horizontal drilling and multi-stage hydraulic fracturing (HF) treatment in Canada. More than 3200 horizontal, multistage wells have been drilled and completed in the Montney since 2008 (Vishkai and Gates, 2019). Although only less than 1% of these stimulated wells are associated with moment magnitude (M_w) <3 earthquakes (Atkinson et al., 2016), the connection between induced earthquakes and strongly controversial issues, such as shale gas, could impact the public and stakeholder perception of clean energy development, as is already apparent from the current perception of deep geothermal energy (Malo et al., 2015). Projects being delayed or abandoned due to public backlash, such as occurred following HF operations in Preston, United Kingdom (Kettletley et al., 2021) or after targeting enhanced geothermal systems in Pohang, South Korea (Ellsworth et al., 2019) and Basel, Switzerland (Majer et al., 2007), represents a direct economic risk to energy developers. More importantly, such backlash can also have wider impacts if deep geothermal energy, natural-gas development as well as carbon capture and storage are prevented from making a timely contribution to climate-change mitigation strategies (Trutnevye and Ejderyan, 2017). Accordingly, fluid-injection-induced seismic hazard assessment and mitigation

planning are necessary steps in tackling global warming. Such seismic hazard analyses and assessments require a comprehensive knowledge of the mechanistic causes of injection-induced shear slips.

In this study, a sensitivity analysis of Montney Formation stiffness (Young's modulus, E) was carried out and its effects on induced-seismicity behaviour and frequency-magnitude distribution were studied. Formation stiffness was selected based on the results of an in-depth machine-learning analysis; this analysis, using a compiled dataset, was carried out on geological and operational parameters throughout the Montney Formation in BC to determine the effect of each parameter on the injection-induced seismicity distribution recorded in BC for shale-gas development. Correlation between induced earthquake hypocentres and sharp changes in seismic tomography (i.e., proxy for formation stiffness, E) has been observed elsewhere (Matzel et al., 2014). Finally, the goal of this paper is to provide insight into the mechanistic reasoning behind such observations. The generic base model (Figure 1a) developed for the common geological setting in northeastern BC uses the new 3-D hybrid lattice and particle-bonded code XSITE™ developed by Itasca Consulting Group, Inc. (Damjanac et al., 2016). The models generated are conceptual but were guided and constrained by reported reservoir characteristics for the Montney Formation in BC. As these models to study the mechanisms of induced seismicity due to fluid injection are designed to be generic, they are not meant to be predictive for any specific site location or set of conditions. By adopting a simpler representation involving a single planar fault, focus was placed on capturing the physics of fluid-pressure perturbation and stress transfer as triggering mechanisms. This model can generate large moment-magnitude events (M_w <3). The input parameters are listed in Table 1. Fluid injection was simulated directly into the fault to gain computational advantages in simulation computing times. This simplified assumption is representative of a scenario where either the borehole, a hydraulic fracture or a discrete fracture network (DFN) intersects the fault and transmits fluid pressure radially into the more permeable

¹The lead author is a 2021 Geoscience BC Scholarship recipient.

This publication is also available, free of charge, as colour digital files in Adobe Acrobat® PDF format from the Geoscience BC website: <http://geosciencebc.com/updates/summary-of-activities/>.

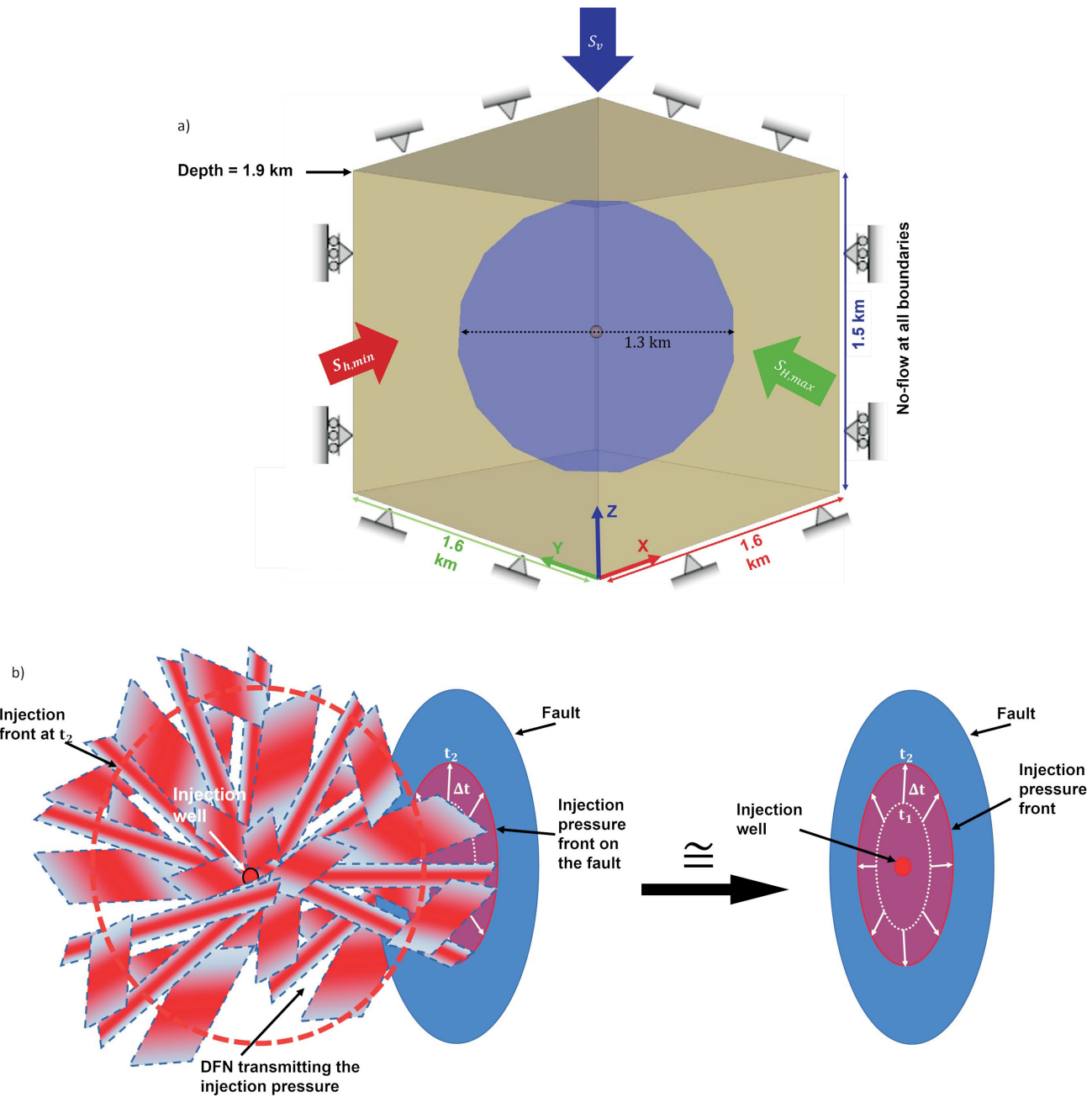


Figure 1. a) Schematic of the XSITE™-generated model of the geometry and boundary conditions characteristic of the Montney Formation in British Columbia. The directions of the principal stresses (S) are shown (note that each stress is parallel to the Cartesian axes of the model as indicated by the matching arrow and axes colours). The geometry and dimension of the fault are shown (strength properties are listed in Table 1). The far-field displacement boundary conditions are fixed at the top and bottom faces (grey symbols), and free to move in the z-direction along the side faces. All the boundaries are impermeable. **b)** Fluid-injection method used for the XSITE modelling. In this scenario, a discrete fracture network (DFN) intersects with a fault, transmitting fluid pressure as a cone-shaped pressure front that radiates outward from the injection point and intersects and perturbs an area of the fault, which increases (Δt) from t_1 (white dotted circle) to t_2 (red dashed circle) with increasing injection time (t).

Table 1. XSite™ model inputs for fluid injection and induced-seismicity simulation, including in situ stress conditions as well as rock-mass and fault properties.

Property	Description
Model geometry	1.6 km × 1.6 km × 1.5 km
Fault radius, initial aperture	$r = 650 \text{ m}$, $a = 0.0001 \text{ m}$
Fault strength properties	$\mu = \tan(27^\circ)^{1, 2}$, $c = 9.5 \text{ MPa}^3$, $T = 2.5 \text{ MPa}^2$
Injection rate at point of intersection with fault ⁴	$q_{\text{inj}} = 0.2 \text{ m}^3/\text{s}^5$
$\partial S_v / \partial Z$ (z axis)	Strike-slip: 25 MPa/km; reverse: 25 MPa/km ^{1, 6}
$\partial S_H / \partial Z$ (y axis)	Strike-slip: 33 MPa/km; reverse: 33 MPa/km; reverse max: 38 MPa/km ^{1, 6}
$\partial S_H / \partial Z$ (x axis)	Strike-slip: 20 MPa/km; reverse: 28 MPa/km ^{1, 6}
Pore-pressure gradient	15 MPa/km ^{1, 6}
Depth at top of the model	1.9 km
Formation density	2600 kg/m ³ ^{1, 2, 7}
Elastic properties	$E = 32 \text{ GPa}$, $v = 0.22^{1, 2, 7}$
Matrix internal friction angle	47° ^{1, 7}
Unconfined compression strength (UCS)	120 MPa ⁷
Fracture toughness	1.25 MPa.m ^{0.5} ^{8, 9}
Tensile strength	1.5 MPa ⁹
Matrix permeability and porosity	$k = 50 \text{ nD}^{1, 10}$, $\Phi = 5\%^{10, 11}$

¹McLellan (2016), Rogers et al. (2014)

²Vaisblat et al. (2019)

³Determined based on sensitivity analysis. Note that the cohesion adds more brittle behaviour to the fault and thus a more sudden release of energy. This value is selected to simulate a conservative scenario (see also Tenthorey and Cox, 2006).

⁴The model is designed to examine the fluid-injection rates, pressures and volumes as experienced by the fault. The implementation of the fluid injection represents a conservative scenario where the borehole or the hydraulic fracture intersects with the discrete fault network (DFN) connected with the fault (see Figure 1b).

⁵Zoback and Kohli (2019)

⁶Fox and Watson (2019); the gradients implemented simulate injection into an over-pressured reservoir. This represents a conservative scenario. The vertical stress gradient is calculated from the average density of the formations from the ground surface to the reservoir depth.

⁷Trican Geological Solutions Ltd. (unpublished report, 2013)

⁸Chen and Wong (2018)

⁹Abdelaziz et al. (2019)

¹⁰Javaheri et al. (2017)

¹¹Vishkai and Gates (2019)

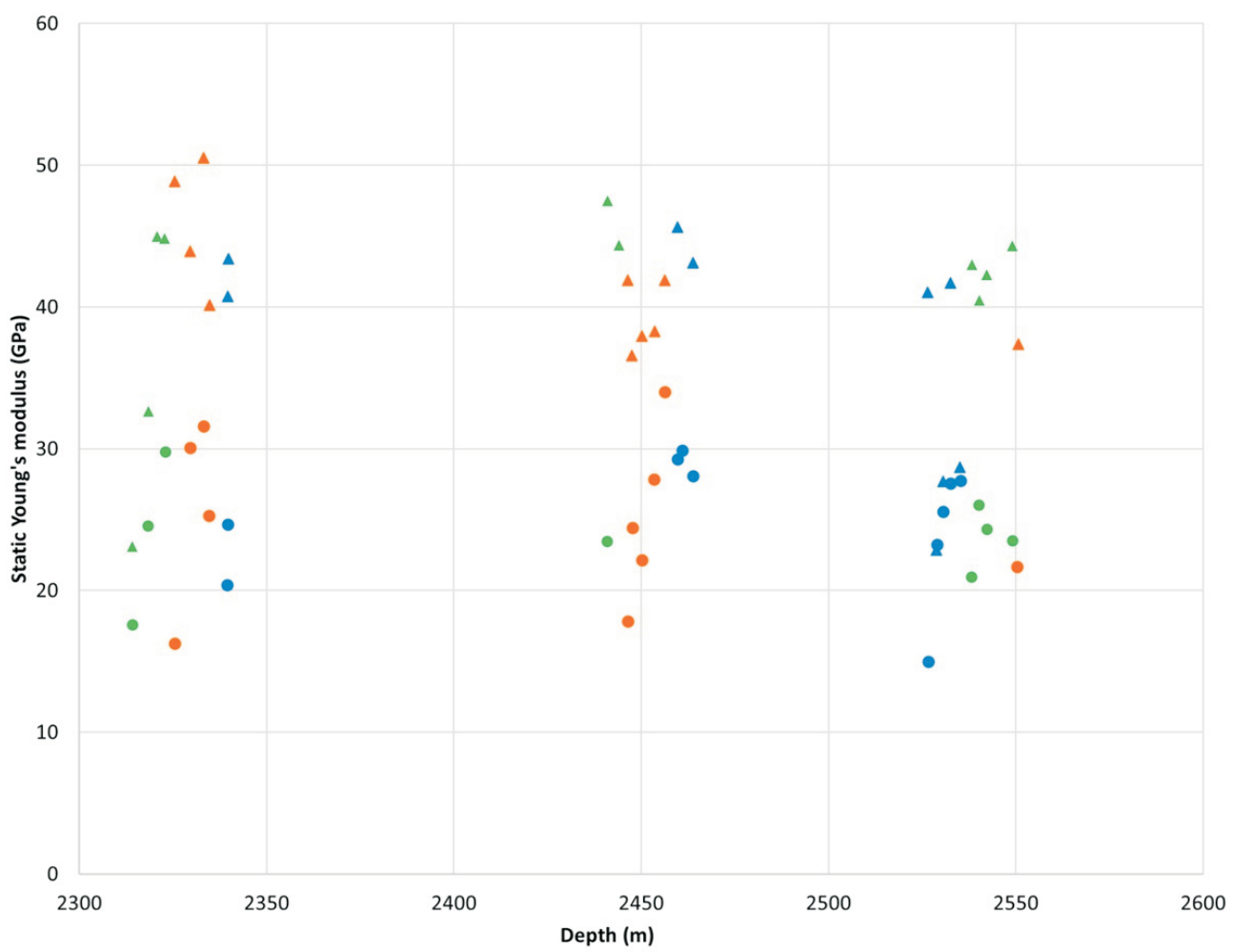
fault (Figure 1b). As the injection continues, the zone of interaction (or the injection pressure front) transmitted to the fault gets larger. The injection-flow rate used was 0.2 m³/s (~75.5 bbl/min), which represents an average value for well stimulations lasting two hours (Zoback and Kohli, 2019).

Results and Discussion

The influence of elastic stiffness (E) on the rock mass hosting a critically stressed fault (a subvertical fault, which is usually hard to detect prior to the operation and hosts M_w<3 events in northeastern BC) was investigated. Rock-mass stiffness is known to be a key influencing factor in fault-slip rockburst hazards encountered in deep mining. Figure 2 shows laboratory-measured Young's modulus (E) values, which range from 16 to 50 GPa, for cores obtained from the Montney Formation at reservoir depths between 2.3 and 2.6 km (Trican Geological Solutions Ltd., unpublished report, 2013). McKean and Priest (2019) reported an even

higher range (42 to 72 GPa), albeit for samples obtained from Montney surface outcrops. To ensure a thorough analysis of the parameter space, five different Young's modulus values were selected covering the reported ranges (see Figure 3). As previously noted, the rock properties were assumed to be homogeneous and isotropic in each model representing a different stiffness of the rock-mass domain.

As the parameter of interest was formation stiffness, the model geometry used assumed the same fault orientation for each model scenario (dip direction of 45°, clockwise from the maximum horizontal stress, and dip angle of 80°). Modelling for this fault orientation considered both the strike-slip and reverse fault stress regimes. Once the in situ stresses and pore pressures are initialized and fluid injection begins, the fluid pressures acting on the fault begin to increase. As the fluid pressure increases, the effective shear



● Vt at zone 1 green ▲ Hz at zone 1 green ● Vt at zone 2 orange ▲ Hz at zone 2 orange ● Vt at zone 3 blue ▲ Hz at zone 3 blue

Figure 2. Laboratory-measured Young's modulus (E) values for rock cores retrieved from the same well in the Montney Formation, north-eastern British Columbia (Trican Geological Solutions Ltd., unpublished report, 2013). The coloured circles and triangles correspond to values of samples tested vertically (Vt) and horizontally (Hz), respectively, relative to the core axis. The colours represent three different zones (1–3) designated as having different rock facies. Abbreviation: GPa, gigapascal.

strength of the fault decreases until the shear-slip criterion is satisfied:

$$\tau - [(\sigma_n - P_f \cdot \tan(27^\circ)) + 9.5] \geq 0$$

where τ refers to shear stress on the fault, the σ_n value is the normal stress on the fault and P_f stands for fluid pressure on the fault. Once this criterion is met, shear slip occurs.

It was observed that as the rock-mass stiffness increases, fluid pressure in the fault becomes greater as there is more resistance to rock-mass deformation:

$$\varepsilon_v = \sigma / K$$

where ε_v is the volumetric strain, the σ value is the mean stress (i.e., the summation of the three principal stresses divided by 3) and K is the bulk modulus. This restricts the ability of the fault aperture to increase, which results in a

higher fluid-pressure gradient (ΔP_f) at the site of the fault, resulting in a larger perturbed area over a shorter injection time:

$$q \propto \Delta P_f \text{ and } q \cdot \Delta t_{inj} = \Delta V = a\pi R^2$$

where q is the fluid flow rate, ΔP_f is the pressure gradient and Δt_{inj} is the injection duration. At the same time, the stiffer rock mass adjacent to the fault provides more confinement (i.e., higher normal stresses) and, therefore, resistance to slip, resulting in more elastic strain energy being stored. Figure 3 illustrates the increasing amount of strain energy stored for a given amount of shear strain (ε_0) as a function of increasing rock-mass shear stiffness (G). It should be noted that the stored elastic strain energy is proportional to the area under the shear stress versus shear strain curve of the rock. Thus, for the same slip area (πR^2)

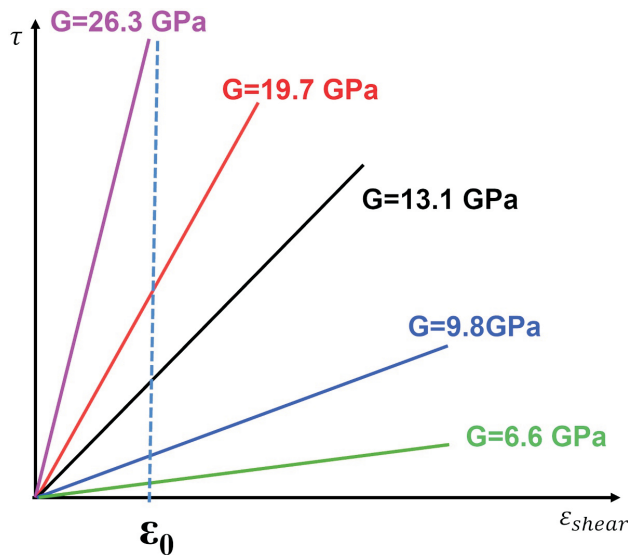


Figure 3. Schematic illustration of the stored elastic strain energy for different rock-mass stiffnesses. The stored elastic strain energy is proportional to the area under the shear stress (τ) versus shear strain curve of the rock. Thus, as rock-mass shear stiffness (G) increases, so does the strain energy stored in the rock mass for the same amount of shear strain (ϵ_0). Abbreviation: GPa, gigapascal.

and displacement (D), it is expected that stiffer rock will result in a larger moment release (M_o ; i.e., $M_o = GD\pi R^2$).

Reverse Fault Far-Field Stress Regime

Figure 4 plots the moment release as a function of injection time for the reverse fault far-field stress-regime boundary condition. The solid lines correspond to the base-case maximum horizontal stress gradient (i.e., 33 MPa/km in Table 1), whereas the dashed lines represent a higher horizontal stress gradient (MPa/km [Reverse max] in Table 1). The latter represents an adjusted gradient that conforms to the observed horizontal stress ratio ($1.1 \leq S_H/S_h \leq 1.4$; see Rogers et al., 2014), but also results in a differential stress (i.e., $S_I - S_3$) that is the same as for the strike-slip stress-regime scenario (Table 1). This facilitates comparison with results for the strike-slip stress-regime scenario presented later. Another important consideration with respect to interpreting this plot, is that XSite is a quasi-static program, whereas fault-slip rupture events are dynamic. To address this limitation, the maximum moment magnitude for a simulation can be calculated by summing the displacement events over the total fluid-injection time, thus treating the displacements as a cluster of cascading events resulting in a single moment magnitude, even though the fault-slip response in the model occurs over an extended injection time. Figure 4

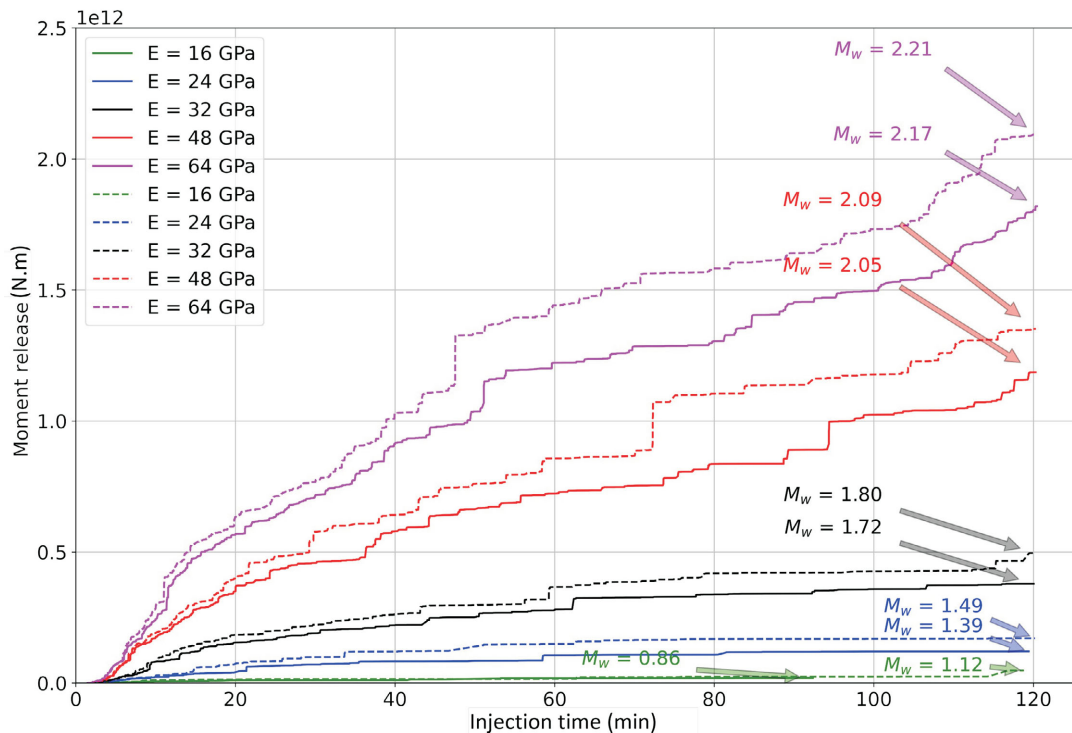


Figure 4. Plot of moment release versus fluid-injection time for models presenting different rock-mass stiffnesses (E). The modelled scenario is for a fault with a dip of 80° and a dip direction of 45° relative to a reverse fault far-field stress regime, assuming either a base-case (solid lines) or maximum (dashed lines) stress gradient. The quasi-static maximum moment magnitude (M_w) is reported for each case. Abbreviations: GPa, gigapascal; N·m, newton-metre.

shows the calculated maximum moment magnitudes (M_w) with arrows pointing at the end of the injection time.

As expected, the overall trend in Figure 4 indicates that higher rock-mass stiffnesses result in the potential for increased moment release and, thus, larger magnitude events. Comparing the solid and dashed lines, the results also suggest that as the differential stress increases, the moment release and maximum event magnitudes increase further. The latter can be explained mechanistically by comparing the shear to normal stress ratio acting on the fault prior to injection, which for the larger differential stress is slightly higher ($\tau/\sigma_n = 0.30$ for the maximum stress gradient compared to $\tau/\sigma_n = 0.18$ for the base-case stress gradient; Figure 5). Consequently, a higher differential stress results in a more critically stressed fault with a larger potential slip area, resulting in larger magnitude events. Viewed another way, a larger differential stress results in a larger stress-

drop potential and therefore larger magnitude events. This is shown in Figure 6, which compares the stress drop with fault slip for the larger differential stress case (blue symbols) to that for the smaller differential stress case (green symbols).

Strike-Slip Far-Field Stress Regime

Figure 6 also includes, for comparison, the average stress drops modelled for the strike-slip far-field stress regime. These are seen to be significantly larger for the same rock-mass stiffness than the stress drops for the reverse fault far-field stress regime, including the maximum stress gradient case. This is further shown in Figure 7, which plots the moment release as a function of simulated injection time for each rock-mass stiffness. Comparing Figure 7 with the similar plot for the reverse fault far-field stress boundary condition (Figure 4), the moment release and event magnitudes

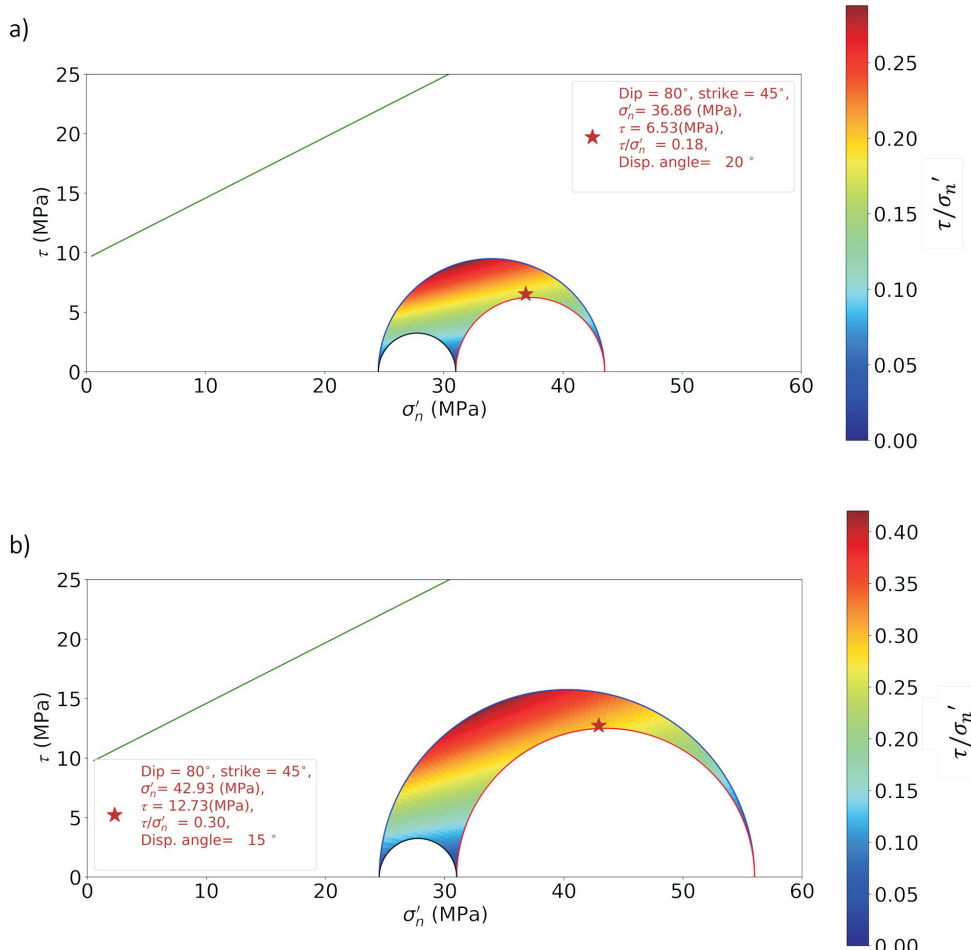


Figure 5. Mohr's circle three dimensional representations of the pre-injection effective normal and shear-stress ratios calculated for a depth of 2.4 km under a reverse fault far-field stress regime for the: **a)** base-case and **b)** maximum stress gradient scenarios. The green line represents the fault-failure envelope (i.e., $\mu = \tan [27^\circ]$ and $c = 9.5$ MPa) and its distance to the Mohr's circle prior to fluid injection into the reservoir. The red star indicates the stress state for a fault with a dip of 80° and a dip direction (Dip D) of 45° relative to the reverse fault far-field stresses. Also reported are the corresponding effective normal stress (σ'_n) and shear stress (τ) ratio (τ/σ'_n) as well as the displacement angle (i.e., the rake angle measured clockwise from the strike). Abbreviation: MPa, megapascal.

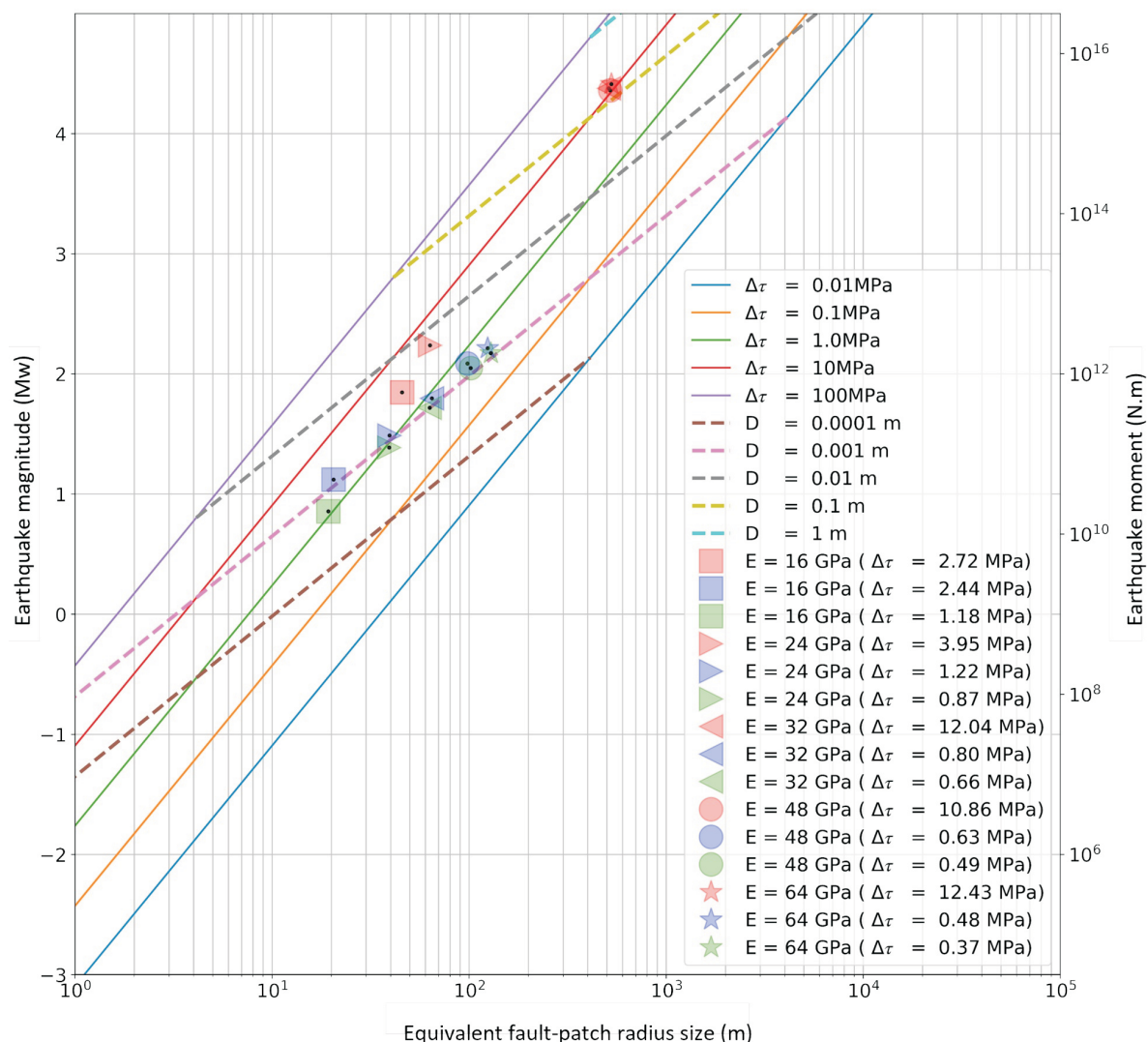


Figure 6. Average stress drop ($\Delta\tau$) and shear displacement (D), and corresponding event magnitude (M_w), derived from the simulation results as a function of rock-mass stiffness (E). The modelled scenario is for a fault with a dip of 80° and a dip direction 45° relative to a reverse fault far-field stress regime and base-case (green symbols) and maximum (blue symbols) stress gradient as well as a strike-slip far-field stress regime (red symbols). These values are based on the maximum induced-seismicity event occurring after 120 minutes of fluid injection. Abbreviations: GPa, gigapascal; MPa, megapascal; N·m, newton-metre.

are significantly higher for the strike-slip far-field stress boundary condition. This relates to the τ/σ_n ratio for the strike-slip far-field stress regime ($\tau/\sigma_n = 0.56$; see Figure 8) being nearly double that of the reverse fault far-field stress regime (see Figure 5). This shows that the strike-slip far-field stress regime, for the assumed fault orientation, results in the fault being more critically stressed, thus requiring a smaller fluid-pressure perturbation to cause slip over a larger area, which results in much larger events.

Figure 7 also shows for the intermediate case of the E = 32 GPa model an interesting deviation from the general trend of increasing moment release that corresponds to increasing rock-mass stiffness. The results for E = 32 GPa show a higher moment release than that recorded in the case of the stiffer E = 48 GPa model. Exploring this further, it

can also be seen that there is a difference related to the injection time when the first sudden energy release and the corresponding moment magnitude ($M_{w,sud}$) is experienced. For the two higher stiffness cases (E = 64 and 48 GPa), this occurs after an injection time of 10 minutes, whereas for the intermediate case (E = 32 GPa) it is 20 minutes, and for the two lower stiffness cases (E = 24 and 16 GPa) it is 30 minutes. As previously discussed, for the same fluid-injection rate, the corresponding fluid pressures acting on the fault increase as the stiffness of the surrounding rock mass increases. Figure 9 shows the bottom-hole fluid pressures during the simulated injection (dashed lines), which confirms these are higher for the two stiffer formations during the first ten minutes of injection. What is seen in the models is that the critical pressure ($P_{f,crit}$; Figure 10) to initiate a

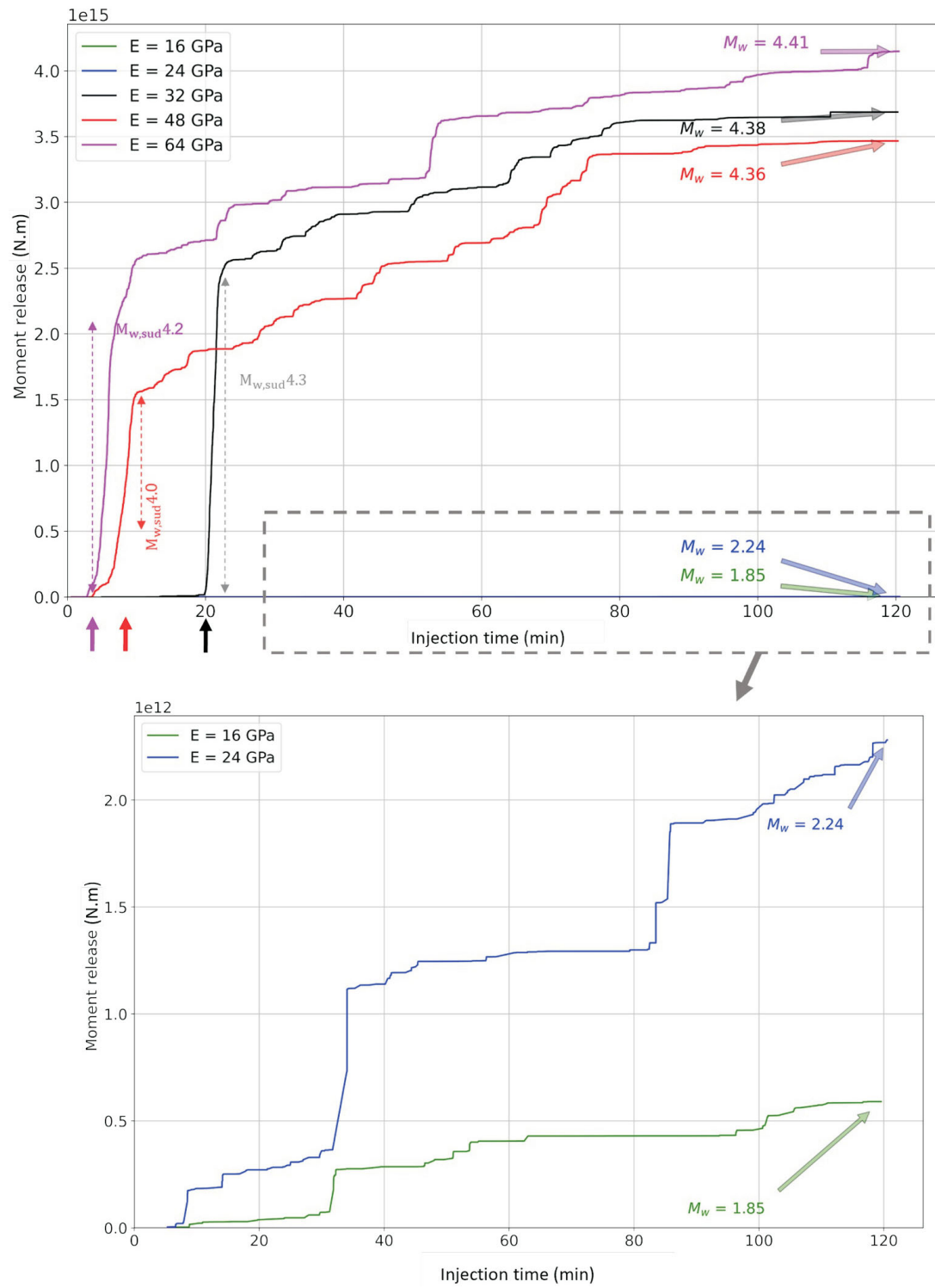


Figure 7. Plot of moment release versus fluid-injection time for models presenting different rock-mass stiffnesses (E). The modelled scenario is for a fault with dip of 80° and a dip direction of 45° relative to a strike-slip far-field stress regime. The quasi-static maximum moment magnitude (M_w) is reported for each case. The dashed arrows represent the sudden energy release and corresponding moment magnitude ($M_{w,sud}$). Panel below the main plot shows moment-release values three orders of magnitude smaller to highlight the details of the response in the case of the lower rock-mass stiffnesses. Note the three orders of magnitude difference in the moment release between the top panel (10^{15} N·m) and the bottom panel (10^{12} N·m). Abbreviations: GPa, gigapascal; N·m, newton-metre.

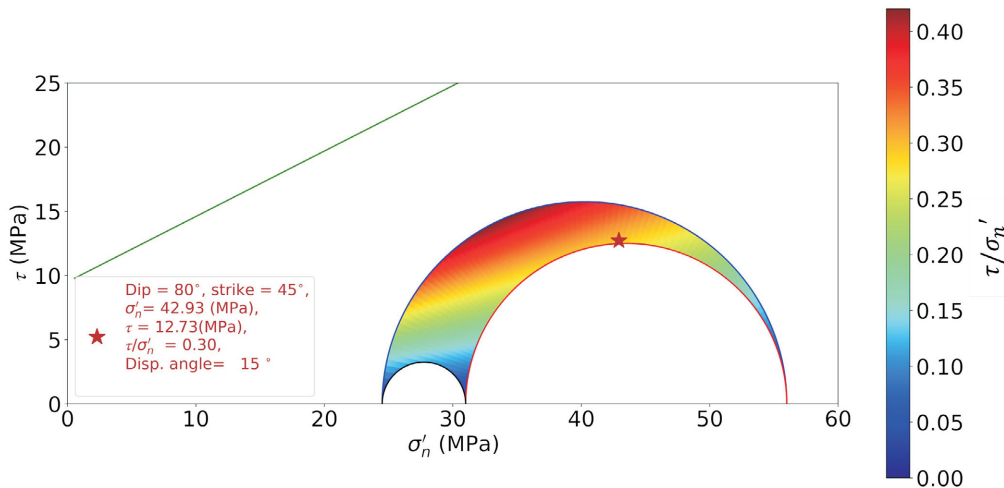


Figure 8. Mohr's circle three-dimensional representation of the pre-injection effective normal and shear-stress ratios calculated for a depth of 2.4 km under a strike-slip far-field stress regime. The green line represents the fault-failure envelope (i.e., $\mu = \tan [27^\circ]$ and $c = 9.5$ MPa) and its distance to the Mohr's circle prior to fluid injection into the reservoir. The red star indicates the stress state for a fault with a dip of 80° and a dip direction (Dip D) of 45° relative to the strike-slip far-field stresses. Also reported are the corresponding effective normal stress (σ'_n) and shear stress (τ) ratio (τ/σ'_n) as well as the displacement angle (i.e., the rake angle measured clockwise from the strike). Abbreviation: MPa, megapascal.

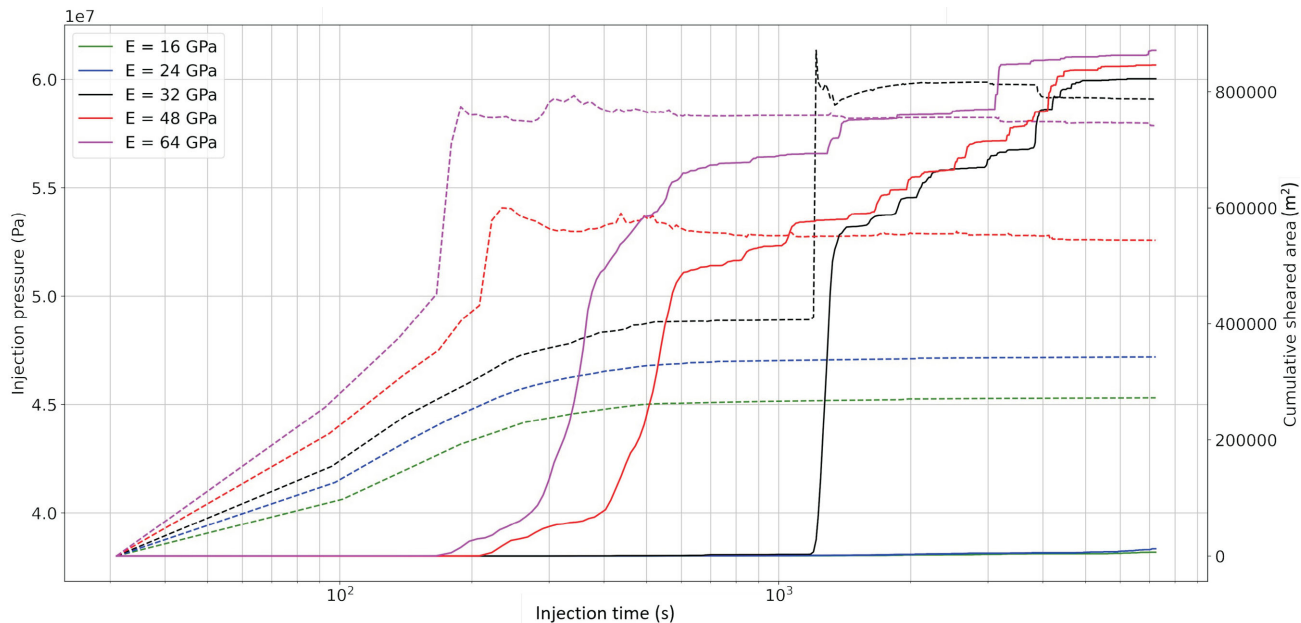


Figure 9. Bottom-hole injection pressures (dashed lines) and cumulative sheared area on the fault (solid lines) as a function of injection time for different rock-mass stiffnesses (E). The modelled scenario is for a fault with a dip of 80° and a dip direction of 45° relative to a strike-slip stress regime. Abbreviations: GPa, gigapascal; Pa, pascal.

fault-slip event is reached with smaller injection volumes for stiffer rocks. At the same time, the smaller injection volumes mean that the areal extent of the increased pore pressures acting on the fault surface is also smaller. Therefore, two factors are at play in the XSite models with respect to the magnitude of the induced-seismicity event (Figure 10):

- the level of stress experienced by the fault in relation to the in situ stress condition and the corresponding stress drop

- the areal extent along the fault experiencing the pore-pressure increase resulting from the fluid injection, which introduces a temporal component related to the injection rate.

As the formation stiffness decreases, it takes a higher fluid pressure acting on the fault to trigger a slip event, which requires a longer injection time and, thus, a larger injection volume can radiate further into the fault, resulting in a

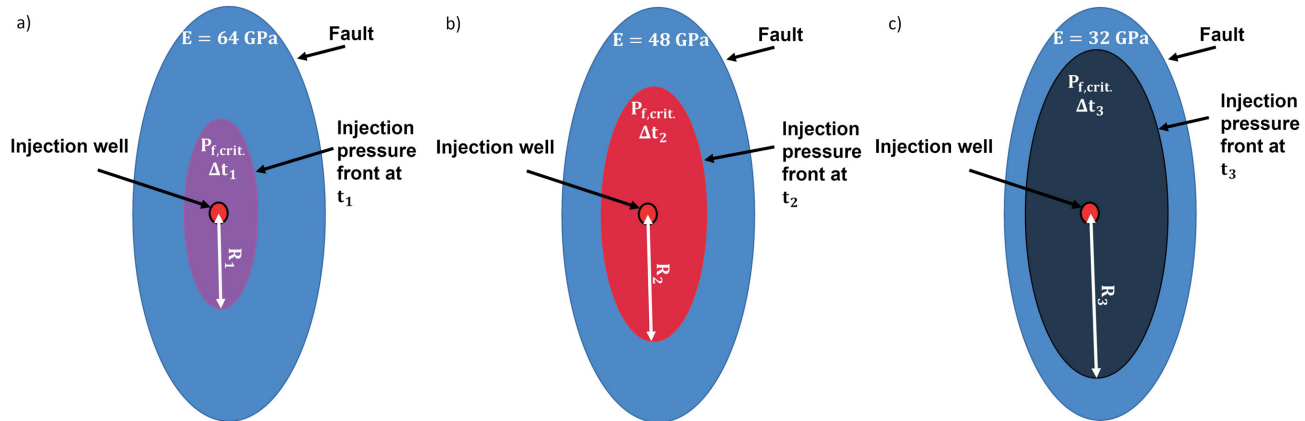


Figure 10. Schematic representation of the fluid-injection front at the time of the first seismic moment release, as observed in Figure 7. The colours of the injection pressure fronts above match those for the rock-mass stiffnesses (E) in Figure 7: **a)** $E = 64$ GPa model (purple); **b)** $E = 48$ GPa model (red); and **c)** $E = 32$ GPa model (black). Each shows the respective area of fluid pressure acting on the fault increasing with injection time (t). The corresponding injection times are, from left to right, $\Delta t_1 \geq \Delta t_2 \geq \Delta t_3$. Abbreviation: GPa, gigapascal.

larger affected fault area. Comparing rock-mass stiffness values $E = 64$ GPa (Figure 10a) and $E = 48$ GPa (Figure 10b), the models are comparable in their sensitivity to the fluid pressure and, therefore, they slip at similar times, with the $E = 64$ case generating a larger slip area (solid lines in Figure 10a) and stress drop as the fault is more critically stressed. In contrast, the $E = 24$ GPa and $E = 16$ GPa models are less critically stressed, and thus require longer injection times (larger injection volumes) for pressures acting on the fault to be sufficient, relative to the corresponding aerial extent of fault weakening, to trigger slip.

It should be noted that although the area on the fault affected by the pore-pressure increase is larger for the lower rock-mass stiffness cases, this does not translate into larger induced-seismicity–event magnitudes. Although the influenced area is larger, the area satisfying the shear-slip criterion is smaller, resulting in a smaller seismic moment.

Thus, in the case of the $E = 32$ GPa model (Figure 10c), an intermediate condition exists. Because the fault in this case is less critically stressed compared to the higher stiffness cases, a longer injection time is possible, allowing more fault area to see an increase in fluid pressure (and decrease in effective stress). At the same time, the rock is still stiff enough to store considerable strain energy. The combined result is that when the induced-seismicity event is triggered, there is more seismic energy suddenly released in the case of the $E = 32$ GPa model than in that of the $E = 48$ GPa model.

Conclusion

The numerical modelling results would suggest that these are wells that are possibly in proximity to faults in higher stiffness rock in a strike-slip far-field stress regime (see Figure 7). Although the XSITE modelled scenario includes numerous simplifications and generalizations, it is interest-

ing to note that the average formation stiffness for the Montney is approximately 32 GPa (Figure 2) and that the crystalline basement rocks would be even stiffer. These results suggest that, when operating in a strike-slip far-field stress regime in stiffer rocks and there are fewer early events of $M_w > 1$ or 2 than expected, this might indicate that strain energy is accumulating toward a large $M_w > 4$ event. Similarly, in the context of a traffic light protocol (e.g., Walters et al., 2015) and seismic hazard, the detection of a M_w 2 event might be more concerning when the formation targeted by the injection, or adjacent to it, is stiffer (e.g., $E > 32$ GPa). These results assume a good hydraulic communication between the injection wells and the fault leading to the observation of early seismicity (i.e., creating a strong correlation between fluid injection and the observation of induced seismicity). It should also be noted that in these results, activity after shut-in is not considered and large induced-seismicity events can occur after well shut-in (e.g., Häring et al., 2008). The next step in this study will be to examine the effect of formation-stiffness anisotropy on injection-induced seismicity behaviour.

Acknowledgments

The authors would like to thank Geoscience BC, Itasca Consulting Group, Inc. and Golder Associates Ltd. for their financial support. They would also like to thank S. Hendi and M. Gorjian for their input and constructive comments on aspects of this work.

References

- Abdelaziz, A., Ha, J., Khair, H.A., Adams, M., Tan, C.P., Musa, I.H. and Grasselli, G. (2019): Unconventional shale hydraulic fracturing under true triaxial laboratory conditions, the value of understanding your reservoir; SPE Annual Technical Conference and Exhibition, Society of Petroleum Engineers, September 30–October 2, 2019, Calgary, Alberta,

- abstract no. SPE-19026-MS, URL <<https://doi.org/10.2118/196026-ms>>.
- Atkinson, G.M., Eaton, D.W., Ghofrani, H., Walker, D., Cheadle, B., Schultz, R., Shcherbakov, R., Tiampo, K., Gu, J., Harrington, R.M., Liu, Y., Van Der Baan, M. and Kao, H. (2016): Hydraulic fracturing and seismicity in the Western Canada Sedimentary Basin; *Seismological Research Letters*, v. 87, no. 3, p. 631–647, URL <<https://doi.org/10.1785/0220150263>>.
- Chen, Q. and Wong, R.C.K. (2018): Mode I and mode II fracture toughness of Montney shale; 52nd U.S. Rock Mechanics/Geomechanics Symposium, June 17–20, 2018, Seattle, Washington, abstract no. ARMA-2018-127, URL <<https://onepetro.org/ARMAUSRMS/proceedings-abstract/ARMA18/All-ARMA18/ARMA-2018-127/124120>> [October 2020].
- Damjanac, B., Detournay, C. and Cundall, P.A. (2016): Application of particle and lattice codes to simulation of hydraulic fracturing; *Computational Particle Mechanics*, v. 3, no. 2, p. 249–261, URL <<https://doi.org/10.1007/s40571-015-0085-0>>.
- Ellsworth, W.L., Giardini, D., Townend, J., Ge, S. and Shimamoto, T. (2019): Triggering of the Pohang, Korea, Earthquake (M_w 5.5) by enhanced geothermal system stimulation; *Seismological Research Letters*, v. 90, no. 5, p. 1844–1858, URL <<https://doi.org/10.1785/0220190102>>.
- Fox, A.D. and Watson, N.D. (2019): Induced seismicity study in the Kiskatinaw Seismic Monitoring and Mitigation Area, British Columbia; report prepared for the BC Oil and Gas Commission, 51 p., URL <<https://www.bcofc.ca/data-reports/reports/?year=2019>> [January 2020].
- Javaheri, A., Dehghanpour, H. and Wood, J. M. (2017): Tight rock wettability and its relationship to other petrophysical properties: a Montney case study; *Journal of Earth Science*, v. 28, no. 2, p. 381–390, URL <<https://doi.org/10.1007/s12583-017-0725-9>>.
- Häring, M.O., Schanz, U., Ladner, F. and Dyer, B.C. (2008): Characterisation of the Basel 1 enhanced geothermal system; *Geothermics*, v. 37, no. 5, p. 469–495, URL <<https://doi.org/10.1016/J.GEOTHERMICS.2008.06.002>>.
- Kettley, T., Verdon, J.P., Butcher, A., Hampson, M. and Craddock, L. (2021): High-resolution imaging of the M_L 2.9 August 2019 earthquake in Lancashire, United Kingdom, induced by hydraulic fracturing during Preston New Road PNR-2 operations; *Seismological Research Letters*, v. 92, no. 1, p. 151–169, URL <<https://doi.org/10.1785/0220200187>>.
- Majer, E.L., Baria, R., Stark, M., Oates, S., Bommer, J., Smith, B. and Asanuma, H. (2007): Induced seismicity associated with enhanced geothermal systems; *Geothermics*, v. 36, no. 3, p. 185–222, URL <<https://doi.org/10.1016/J.GEOTHERMICS.2007.03.003>>.
- Malo, M., Moutenet, J.-P., Bédard, K. and Raymond, J. (2015): Public awareness and opinion on deep geothermal energy in the context of shale gas exploration in the Province of Québec, Canada; in *Proceedings of the World Geothermal Congress*, April 19–25, 2015, Melbourne, Australia, 8 p.
- Matzel, E., Templeton, D., Petersson, A. and Goebel, M. (2014): Imaging the Newberry EGS site using seismic interferometry; in *Proceedings of the Thirty-Ninth Workshop on Geothermal Reservoir Engineering*, February 24–26, 2014, Stanford, California, 4 p.
- McGarr, A. (2014): Maximum magnitude earthquakes induced by fluid injection; *Journal of Geophysical Research: Solid Earth*, v. 119, no. 2, p. 1008–1019, URL <<https://doi.org/10.1002/2013JB010597>>.
- McKean, S.H. and Priest, J.A. (2019): Multiple failure state triaxial testing of the Montney Formation; *Journal of Petroleum Science and Engineering*, v. 173, p. 122–135, URL <<https://doi.org/10.1016/J.PETROL.2018.09.004>>.
- McLellan, P. (2016): Geomechanical characterization of the Farrell Creek Montney reservoir, northeast British Columbia; SPE Workshop: the Montney Play; Society of Petroleum Engineers, October 18, 2016, Calgary, Alberta, Canada, workshop presentation.
- National Energy Board, BC Oil and Gas Commission, Alberta Energy Regulator and BC Ministry of Natural Gas Development (2013): Energy briefing note: the ultimate potential for unconventional petroleum from the Montney Formation of British Columbia and Alberta; National Energy Board, BC Oil and Gas Commission, Alberta Energy Regulator and BC Ministry of Natural Gas Development, briefing note, 23 p., URL <<https://www.cer-rec.gc.ca/en/data-analysis/energy-commodities/natural-gas/report/ultimate-potential-montney-formation/the-ultimate-potential-unconventional-petroleum-from-montney-formation-british-columbia-alberta-energy-briefing-note.html>> [September 2020].
- Rogers, S., McLellan, P. and Webb, G. (2014): Investigation of the effects of natural fractures and faults on hydraulic fracturing in the Montney Formation, Farrell Creek gas field, British Columbia; International Discrete Fracture Network Engineering Conference, October 1–13, 2014, Vancouver, British Columbia, art. 224, 12 p.
- Tenthorey, E. and Cox, S.F. (2006): Cohesive strengthening of fault zones during the interseismic period: an experimental study; *Journal of Geophysical Research: Solid Earth*, v. 111, no. B9, art. B09202, 14 p., URL <<https://doi.org/10.1029/2005JB004122>>.
- Trutnevyte, E. and Ejderyan, O. (2017): Managing geoenergy-induced seismicity with society; *Journal of Risk Research*, v. 21, no. 10, p. 1287–1294, URL <<https://doi.org/10.1080/13669877.2017.1304979>>.
- Vaisblat, N., Shokri, A.R., Ayrancı, K., Harris, N. and Chalaturnyk, R.J. (2019): Significance of rock compositional control on geomechanical properties and hydraulic fracturing of the Montney Formation, Western Canadian Basin; Asia Pacific Unconventional Resources Technology Conference, November 18–19, 2019, Brisbane, Australia, p. 752–784, URL <<https://doi.org/10.15530/ap-urtec-2019-198199>>.
- Vishkai, M. and Gates, I. (2019): On multistage hydraulic fracturing in tight gas reservoirs: Montney Formation, Alberta, Canada; *Journal of Petroleum Science and Engineering*, v. 174, p. 1127–1141, URL <<https://doi.org/10.1016/J.PETROL.2018.12.020>>.
- Walters, R.J., Zoback, M.D., Baker, J.W. and Beroza, G.C. (2015): Characterizing and responding to seismic risk associated with earthquakes potentially triggered by fluid disposal and hydraulic fracturing; *Seismological Research Letters*, v. 86, no. 4, p. 1110–1118, URL <<https://doi.org/10.1785/0220150048>>.
- Zoback, M. and Kohli, A. (2019): *Unconventional Reservoir Geomechanics: Shale Gas, Tight Oil, and Induced Seismicity*; Cambridge University Press, Cambridge, United Kingdom, 492 p., URL <<https://doi.org/10.1017/9781316091869>>.

